


 Cite this: *Chem. Commun.*, 2024, 60, 7713

 Received 17th May 2024,  
 Accepted 11th June 2024

DOI: 10.1039/d4cc02372b

rsc.li/chemcomm

# Inverse kinetic isotope effect of ammonia decomposition over Ru/CeO<sub>2</sub> using deuterated ammonia†

 Takuya Suguro, Fuminao Kishimoto, \* Sota Kuramoto, William J. Movick and Kazuhiro Takanabe \*

**This study investigated the ammonia decomposition mechanism over Ru/CeO<sub>2</sub>. Isotopic tests using ND<sub>3</sub> revealed that the rate-determining step involves adsorbed nitrogen atoms on Ru. Moreover, an inverse kinetic isotope effect where ND<sub>3</sub> decomposition was faster than NH<sub>3</sub> was clearly observed. The origin of the inverse effect was explained by the lower D coverage on the catalyst surface compared to H coverage for mitigating the inhibition of ND<sub>3</sub> activation.**

Green hydrogen (H<sub>2</sub>) generated using renewable energy is attracting attention as a next-generation fuel that could replace fossil fuels.<sup>1–4</sup> Studies have been examining the chemical conversion of H<sub>2</sub> into the form of a hydrogen carrier, such as ammonia (NH<sub>3</sub>), which is easily liquefied, transported, and stored. A supply chain is envisioned in which green H<sub>2</sub> is produced using renewable energy, chemically converted to NH<sub>3</sub>, and then transported to urban areas for use as fuel. When NH<sub>3</sub> is used as a fuel, there are two possible cases: N<sub>2</sub> and H<sub>2</sub>O production by direct transformation of NH<sub>3</sub> and NH<sub>3</sub> decomposition reaction to extract pure hydrogen and then using that as a fuel. Thanks to recent research on combustion equipment development, NH<sub>3</sub> combustion engines with reduced NO<sub>x</sub> emissions are being realized.<sup>5</sup> On the other hand, the NH<sub>3</sub> decomposition process leads to pure H<sub>2</sub>, which can be widely used for conventional fuel cells or as chemical feedstocks.

NH<sub>3</sub> can be decomposed using various metals.<sup>6–11</sup> Ru shows outstanding performance for NH<sub>3</sub> decomposition under high NH<sub>3</sub> concentrations and shows optimal dissociative N<sub>2</sub> adsorption energy.<sup>8–12</sup> The various types of support materials were investigated for enhancing the NH<sub>3</sub> decomposition performance over the Ru catalyst, *e.g.* CeO<sub>2</sub><sup>10,11</sup> (with PrO<sub>x</sub><sup>13</sup>), MgAl<sub>2</sub>O<sub>4</sub>,<sup>14</sup> Al<sub>2</sub>O<sub>3</sub>,<sup>15</sup> carbon nanotubes,<sup>16–18</sup> carbon nanofiber,<sup>19</sup> SiC,<sup>20</sup>

C12A7:e<sup>−</sup> (ref. 21), and MgO<sup>8,9</sup> with various exposed crystal facets.<sup>22</sup>

The differences in ammonia decomposition kinetics in terms of the exposed facets of Ru<sup>23–25</sup> have been investigated. Egawa *et al.* demonstrated NH<sub>3</sub> and ND<sub>3</sub> isotope tests at ultra-low ammonia pressure (~10<sup>−5</sup> kPa) over single-crystal surfaces of Ru (1110) and Ru (001), which showed the normal kinetic isotope effect (NH<sub>3</sub> decomposition occurred faster than ND<sub>3</sub> decomposition).<sup>23</sup> The rate-determining step was N–H bond cleavage under such low ammonia pressure conditions. Tsai *et al.* demonstrated a temperature dependence of the reaction rate of Ru (0001) and showed that the associative desorption of N<sub>2</sub> was the rate-determining step below 377 °C. The rate-determining step changed to cleavage of the N–H bonding at higher temperature.<sup>24</sup> A study using density functional theory predicted that the formation of the molecular nitrogen would be the rate-determining step with Ru (0001) and Ru (111).<sup>25</sup> The Temkin–Pyzhev model is widely accepted to express the ammonia decomposition kinetics and assumes that associative N<sub>2</sub> desorption step is the rate-determining step.<sup>15,26</sup> This model fits well with conditions where reaction inhibition by hydrogen is observed at low temperatures or high pressures.<sup>27</sup> However, several other models of reaction kinetics show different rate-determining steps.<sup>28–30</sup> Armenise *et al.* reported a microkinetic analysis of ammonia decomposition with a Langmuir–Hinshelwood approach and modeled the reaction to predict an integral reactor by assuming the rate-determining step to be N<sub>2</sub> desorption and strong hydrogen and ammonia adsorption.<sup>31</sup>

Although isotope experiments are a powerful tool for examining rate-determining steps, to our best knowledge, there are hardly any reports on isotope tests in the pressure range where reaction inhibition by adsorbed molecules is observed. Antunes *et al.* demonstrated the normal kinetic isotope effect over supported Ru/Al<sub>2</sub>O<sub>3</sub> at an ammonia partial pressure of 1.5 Pa.<sup>32</sup> However, different ammonia partial pressures should result in different catalyst surface coverage and thus different kinetics.<sup>12</sup>

Department of Chemical System Engineering, School of Engineering,  
 The University of Tokyo, 7-3-1 Hongo, Bunkyo-ku, Tokyo, Japan.

E-mail: kfuminao@chemsys.t.u-tokyo.ac.jp, takanabe@chemsys.t.u-tokyo.ac.jp

† Electronic supplementary information (ESI) available: Experimental methods, partial pressure dependence, and fitting result. See DOI: <https://doi.org/10.1039/d4cc02372b>



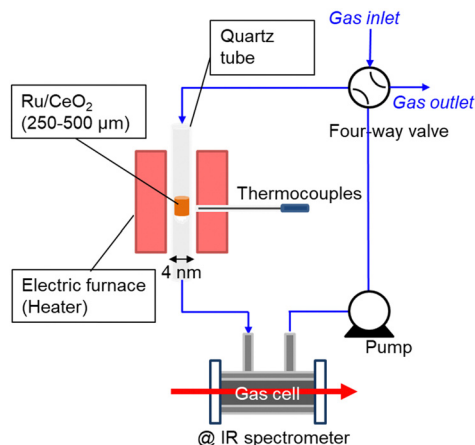


Fig. 1 Schematic diagram of the closed recirculation batch system for catalytic ammonia decomposition.

Therefore, this paper reports the kinetic isotope effect of ammonia decomposition reaction using  $\text{ND}_3$  at 1 kPa over Ru/CeO<sub>2</sub> (TEM image is shown in Fig. S1, ESI<sup>†</sup>). Fig. 1 shows the experimental setup used for  $\text{NH}_3$  decomposition. The catalyst bed was placed in a quartz tube with an internal diameter of 4 mm and heated with an electric furnace. The temperature of the cylindrical catalyst bed was measured using a thermocouple located outside the quartz tube at the catalyst bed. The catalytic reaction was performed with a closed circulation configuration (gradient-less batch reactor). The quantity of the accumulated  $\text{NH}_3$  gas was estimated from the infrared absorption spectra passing through the in-line gas cell.

Fig. S2(a) (ESI<sup>†</sup>) shows typical results of the  $\text{NH}_3$  decomposition at various temperatures over a supported Ru/CeO<sub>2</sub> catalyst. Deposition of colloidal Ru nanoparticles (mean particle size  $\sim 4$  nm) on the CeO<sub>2</sub> support was employed to eliminate particle-size effects among the different samples. For tests at higher temperature, the Ru-deposited CeO<sub>2</sub> catalyst was diluted with pristine CeO<sub>2</sub> to control the reaction rate. As shown in Fig. S2(b) (ESI<sup>†</sup>), the  $\text{NH}_3$  decomposition rates were obtained from the slope of the line connecting the several plotted points in Fig. S2(a) (ESI<sup>†</sup>).

Fig. 2 shows the partial pressure dependence of ammonia decomposition over the supported Ru/CeO<sub>2</sub> catalyst. The apparent kinetic order with respect to  $\text{NH}_3$  partial pressure was 0.23 at 200 °C, which gradually increased with the temperature, reaching 0.62 at 400 °C. Next,  $\text{N}_2$  was introduced into the initial gas composition to study its partial pressure dependence on the reaction rate. The  $\text{N}_2$  partial pressure was insensitive to the  $\text{NH}_3$  decomposition rate at both 200 and 400 °C (Fig. 2(b)).

$\text{H}_2$  introduction caused a decrease of the ammonia decomposition rate at 200–400 °C. Substantially negative order of  $-0.66$  on  $\text{H}_2$  partial pressure was observed at 200 °C (Fig. 3). The inhibition effects by  $\text{H}_2$  became less severe with increasing temperature, reaching  $-0.35$  at 400 °C.

Elementary reaction steps were examined for detailed analysis of the kinetics as follows:

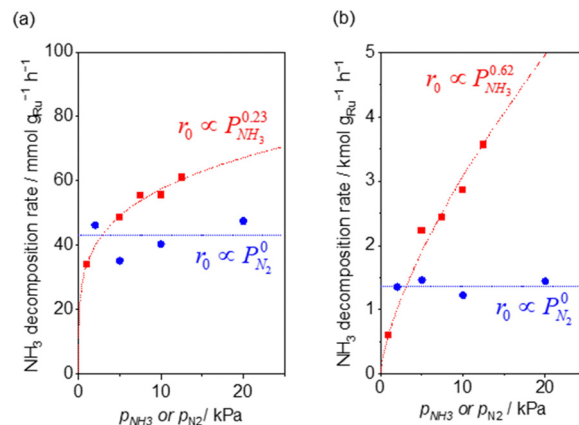
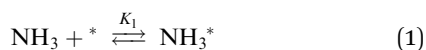


Fig. 2  $\text{NH}_3$  (red square) and  $\text{N}_2$  (blue circle) pressure dependence of ammonia decomposition rates (a) over 0.1 mg of 5 wt% Ru/CeO<sub>2</sub> diluted with 9.9 mg of CeO<sub>2</sub> within pellets at 200 °C and (b) over 1 mg pellets of 10 $\times$  further dilution with CeO<sub>2</sub> within the pellets at 400 °C. Initial conditions:  $\sim 0.5$  kPa  $\text{NH}_3$  balanced with Ar, total 101 kPa. Raw data are shown in Fig. S3 and S4 (ESI<sup>†</sup>).

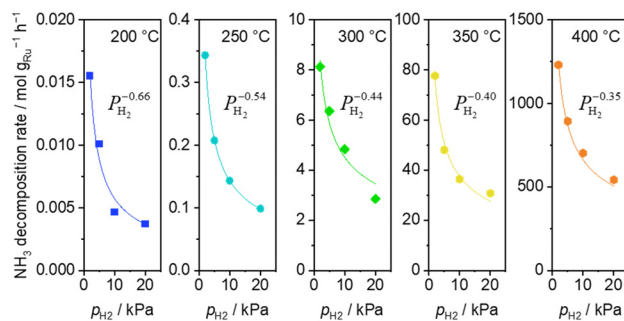
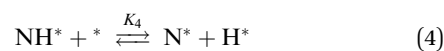
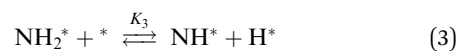
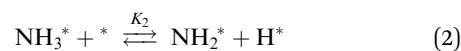


Fig. 3  $\text{H}_2$  pressure dependence of ammonia decomposition rates over 0.1 mg of 5 wt% Ru/CeO<sub>2</sub> diluted with 9.9 mg of CeO<sub>2</sub> within the pellets at 200 (blue square), 250 (light blue circle) and 300 °C (green diamond) and over 1 mg pellets of 10 $\times$  further dilution with CeO<sub>2</sub> within pellets at 350 (yellow pentagon) and 400 °C (orange pentagon) (5 kPa  $\text{NH}_3$ , balanced by Ar). Raw data are shown in Fig. S5 (ESI<sup>†</sup>).



in which \* denotes active sites, and  $k_i$  and  $K_i$  represent the reaction constant and adsorption equilibrium constant of reaction  $i$ , respectively.

Fig. 4(a) shows the Arrhenius plot of  $\text{NH}_3$  and  $\text{ND}_3$  decomposition over the supported Ru/CeO<sub>2</sub> catalyst. Notably, an



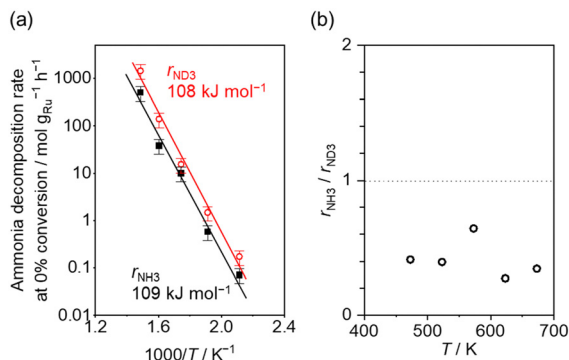


Fig. 4 (a) Arrhenius plot of  $\text{NH}_3$  (black square) and  $\text{ND}_3$  (red circle) decomposition over 0.1 mg of 5 wt% Ru/CeO<sub>2</sub> diluted with 9.9 mg of CeO<sub>2</sub> within pellets below 300 °C and over 1 mg pellets of 10× further dilution with CeO<sub>2</sub> within pellets above 400 °C. The initial gas ratio was Ar :  $\text{NH}_3$  = 100 : 1 kPa or Ar/ $\text{ND}_3$  = 100 : 1 kPa. The raw data are shown in Fig. S6–S10 (ESI†). Error bars: 34.1% (1σ of Gaussian distribution). (b) Ratio of  $\text{NH}_3$  decomposition rate,  $r_{\text{NH}_3}$ , to  $\text{ND}_3$  decomposition rate,  $r_{\text{ND}_3}$ , as a function of reaction temperature. Averaged  $r_{\text{NH}_3}/r_{\text{ND}_3}$  was 0.414 with a standard error of 0.062 (standard deviation = 0.139).

inverse kinetic isotope effect was observed at all temperatures, where the decomposition rate of  $\text{ND}_3$  was greater than that of  $\text{NH}_3$ . The apparent activation energy for  $\text{NH}_3$  and  $\text{ND}_3$  decomposition was almost identical (109 and 108 kJ mol<sup>-1</sup>). If N–H bond breaking (steps (2–4)) is involved in the rate-determining step, the activation energies should obviously be different. Therefore, the identical activation energy suggested that the rate-determining step should be steps (1), (5), (6) and (7), and most likely for associative N–N bonding formation (step (5)).

Fig. 4(b) shows the ratio of  $\text{NH}_3$  and  $\text{ND}_3$  decomposition rates ( $r_{\text{NH}_3}/r_{\text{ND}_3}$ ) in the Arrhenius expression. The degree of kinetic isotope effect was independent of the reaction temperature and was almost constant (~0.5). Aika and Ozaki studied the inverse kinetic isotope effect on  $\text{NH}_3$  synthesis (*i.e.*, reverse reaction of  $\text{NH}_3$  decomposition). Strong inverse kinetic isotope effects were observed in the reaction of  $\text{H}_2$  and  $\text{D}_2$  with  $\text{N}_2$  over iron,<sup>33,34</sup> molybdenum-based,<sup>35</sup> or even Ru-based<sup>36,37</sup> catalysts. The inverse kinetic isotope effects were explained by the larger equilibrium constant for  $\text{ND}_3$  decomposition relative to  $\text{NH}_3$  decomposition, which increased the empty sites for  $\text{N}_2$  activation.

Based on elementary steps (1)–(7), the overall reaction rate can be expressed as follows with an assumption of nitrogen triple bond formation in step (5) as the rate-determining step (adopted from Stoltze<sup>38</sup>).

$$-r_{\text{NH}_3} = r_5 = k_5^+ K_1^2 K_2^2 K_3^2 K_4^2 K_7^{-3} \left( P_{\text{NH}_3}^2 P_{\text{H}_2}^{-3} - \frac{P_{\text{N}_2}}{K_g} \right) \theta_*^2 \quad (8)$$

$$\theta_* = \left[ 1 + \left( \frac{P_{\text{N}_2}}{K_6} \right)_{\text{N}_2} + \left( \frac{K_1 K_2 K_3 K_4 P_{\text{NH}_3}}{K_7^{1.5} P_{\text{H}_2}^{1.5}} \right)_{\text{N}} + \left( \frac{K_1 K_2 K_3 P_{\text{NH}_3}}{K_7 P_{\text{H}_2}} \right)_{\text{NH}} + \left( \frac{K_1 K_2 P_{\text{NH}_3}}{K_7^{0.5} P_{\text{H}_2}^{0.5}} \right)_{\text{NH}_2} + (K_1 P_{\text{NH}_3})_{\text{NH}_3} + (K_7^{0.5} P_{\text{H}_2}^{0.5})_{\text{H}} \right]^{-1} \quad (9)$$

$K_g$  and  $\theta_*$  represent the equilibrium constant of the overall ammonia decomposition reaction at given conditions and the fraction of empty sites, respectively. The first assumption is that H is the most abundant reactive intermediate (MARI) because of the negative partial pressure dependence on  $\text{H}_2$ . However, if the terms other than hydrogen are eliminated from eqn (9), the partial pressure dependence of the reaction rate on hydrogen becomes negative fourth order, which is too large compared to the experimental results.

$$-r_{\text{NH}_3} = \frac{k_5^+ K_1^2 K_2^2 K_3^2 K_4^2 P_{\text{NH}_3}^2}{K_7^2 P_{\text{H}_2}^4} \quad (10)$$

Assuming  $\text{NH}_3$  as the MARI, the order of the partial pressure dependence on  $\text{H}_2$  is still minus three. To be consistent with the zero order of  $\text{N}_2$  and the slightly negative order of  $\text{H}_2$  demonstrated by experiments, we derived the rate expression by assuming  $\text{NH}$  or  $\text{NH}_2$  species as the MARI, respectively:

$$-r_{\text{NH}_3} = \frac{k_5^+ K_4^2}{K_7 P_{\text{H}_2}} \quad (11)$$

or

$$-r_{\text{NH}_3} = \frac{k_5^+ K_3^2 K_4^2}{K_7^2 P_{\text{H}_2}^2} \quad (12)$$

However, none of these partial pressure dependencies fully match the experimental results ( $\text{NH}_3$  order: 0.23 to 0.62,  $\text{H}_2$  order: -0.66 to -0.35,  $\text{N}_2$  order: ~0), suggesting that the balance of these adsorbed species on the surface affects the reaction rate.

From the experimental results, both the ammonia and hydrogen orders increased with increasing temperature. Typically, the surface reaction intermediates decreased as the temperature increases, meaning that the coverage term,  $\theta_*$ , becomes closer to zero at higher temperatures. Therefore, based on eqn (8), the dependence on ammonia partial pressure increases with increasing temperature under ammonia partial pressure. On the other hand, the effect of reaction inhibition by intentionally introduced hydrogen weakened as the temperature increased. This change can be explained by the change in MARI with increasing temperature. At high temperatures, MARI approaches N, and the apparent hydrogen partial pressure dependence is expected to approach zero, as shown in the equation below.

$$-r_{\text{NH}_3} = k_5^+ \quad (13)$$

From the rate expression as eqn (11) or (12), one possibility for explanation of the inverse kinetic isotope effect is the difference of the equilibrium constant of  $\text{H}_2$  or  $\text{D}_2$  adsorption/desorption ( $K_7$ ). Kellner and Bell studied  $\text{H}_2/\text{D}_2$  isotope effects on Fischer–Tropsch synthesis over supported Ru catalysts.<sup>39</sup> They calculated the equilibrium constant of  $\text{H}_2$  and  $\text{D}_2$  adsorption on Ru from vibrational frequencies for molecular and atomically adsorbed  $\text{H}_2$  and  $\text{D}_2$  (derivation is shown in the ESI†). The ratio of the equilibrium constants of  $\text{D}_2$  adsorption and that of  $\text{H}_2$  adsorption ( $K_{7,\text{D}}/K_{7,\text{H}}$ ) was less than 1



between 180 °C and 270 °C, or the equilibrium shifted more toward desorption for D<sub>2</sub> than for H<sub>2</sub>. Based on rate expression (11) or (12), lower  $K_7$  leads to a higher overall reaction rate due to more active surface species for the forward reaction (less inhibition). Therefore, the difference in the adsorption equilibrium constants of H<sub>2</sub> and D<sub>2</sub> can be one possible explanation for the inverse kinetic isotope effect in the NH<sub>3</sub> decomposition reaction over the Ru/CeO<sub>2</sub> catalyst observed in this study, suggesting that the secondary kinetic isotope effect appears inversely.

In conclusion, kinetic analysis using Ru/CeO<sub>2</sub> revealed that comparable apparent activation energies between NH<sub>3</sub> and ND<sub>3</sub> decomposition reactions ( $\sim 108$  kJ mol<sup>-1</sup>) were obtained with an inverse kinetic isotope effect ( $r_{\text{NH}_3}/r_{\text{ND}_3} \sim 0.5$ ). The kinetic orders were zero with respect to N<sub>2</sub> partial pressure and negative with respect to H<sub>2</sub> partial pressure on the NH<sub>3</sub> decomposition rate. The results suggest that the rate-determining step does not involve N–H or N–D bond dissociation, but it likely involves N–N triple bond formation, of which the rate is strongly perturbed by the surface H(D) adsorption equilibrium from H<sub>2</sub> and D<sub>2</sub> to the Ru surface. The adsorption equilibrium constant for D<sub>2</sub> is smaller than that for H<sub>2</sub>, resulting in lower D coverage than H coverage, which is advantageous for high N\* coverage. It can be concluded that the observed isotope effect was the secondary kinetic isotope effect inversely influenced by H(D) surface coverage. A more comprehensive understanding of the kinetics can be attained with further studies on isotope effects under diverse conditions.

This work was financially supported by the Mohammed bin Salman Center for Future Science and Technology for Saudi-Japan Vision 2030 at The University of Tokyo (MbSC2030), and the Science and Technology Research Partnership for Sustainable Development (SATREPS) in collaboration between the Japan Science and Technology Agency (JST, JPMJSA2104) and Japan International Cooperation Agency (JICA).

## Data availability

The data supporting this article have been included as part of the ESI.† Raw data for each experiment is available by contacting the corresponding author.

## Conflicts of interest

There are no conflicts to declare.

## Notes and references

- 1 A. Klerke, C. H. Christensen, J. K. Nørskov and T. Vegge, *J. Mater. Chem.*, 2008, **18**, 2304–2310.
- 2 S. Mukherjee, S. V. Devaguptapu, A. Sviripa, C. R. F. Lund and G. Wu, *Appl. Catal., B*, 2018, **226**, 162–181.
- 3 K. E. Lamb, M. D. Dolan and D. F. Kennedy, *Int. J. Hydrogen Energy*, 2019, **44**, 3580–3593.
- 4 N. Morlanés, S. P. Katikaneni, S. N. Paglieri, A. Harale, B. Solami, S. M. Sarathy and J. Gascon, *Chem. Eng. J.*, 2021, **408**, 127310.
- 5 J. S. Cardoso, V. Silva, R. C. Rocha, M. J. Hall, M. Costa and D. Eusébio, *J. Cleaner Prod.*, 2021, **296**, 126562.
- 6 S. Brunauer, K. S. Love and R. G. Keenan, *J. Am. Chem. Soc.*, 1942, **64**, 751–758.
- 7 J. C. Ganley, F. S. Thomas, E. G. Seebauer and R. I. Masel, *Catal. Lett.*, 2004, **96**, 117–122.
- 8 C. Chen, K. Wu, H. Ren, C. Zhou, Y. Luo, L. Lin, C. Au and L. Jiang, *Energy Fuels*, 2021, **35**, 11693–11706.
- 9 T. Su, B. Guan, J. Zhou, C. Zheng, J. Guo, J. Chen, Y. Zhang, Y. Yuan, W. Xie, N. Zhou, H. Dang, B. Xu and Z. Huang, *Energy Fuels*, 2023, **37**, 8099–8127.
- 10 I. Lucentini, A. Casanovas and J. Llorca, *Int. J. Hydrogen Energy*, 2019, **44**, 12693–12707.
- 11 I. Lucentini, G. García Colli, C. D. Luzi, I. Serrano, O. M. Martínez and J. Llorca, *Appl. Catal., B*, 2021, **286**, 119896.
- 12 A. Boisen, S. Dahl, J. K. Nørskov and C. H. Christensen, *J. Catal.*, 2005, **230**, 309–312.
- 13 K. Yamazaki, M. Matsumoto, M. Ishikawa and A. Sato, *Appl. Catal., B*, 2023, **325**, 122352.
- 14 D. Szmigielski, W. Raróg-Pilecka, E. Miśkiewicz, Z. Kaszkur and Z. Kowalczyk, *Appl. Catal., A*, 2004, **264**, 59–63.
- 15 W. Zheng, J. Zhang, H. Xu and W. Li, *Catal. Lett.*, 2007, **119**, 311–318.
- 16 S. F. Yin, B. Q. Xu, W. X. Zhu, C. F. Ng, X. P. Zhou and C. T. Au, *Catal. Today*, 2004, **93**, 27–38.
- 17 S. F. Yin, Q.-H. Zhang, B.-Q. Xu, W.-X. Zhu, C.-F. Ng and C.-T. Au, *J. Catal.*, 2004, **224**, 384–396.
- 18 S. F. Yin, B. Q. Xu, S. J. Wang, C. F. Ng and C. T. Au, *Catal. Lett.*, 2004, **96**, 113–116.
- 19 S. Armenise, L. Roldán, Y. Marco, A. Monzón and E. García-Bordejé, *J. Phys. Chem. C*, 2012, **116**, 26385–26395.
- 20 M. Pinzón, A. Romero, A. de Lucas Consuegra, A. R. de la Osa and P. Sánchez, *J. Ind. Eng. Chem.*, 2021, **94**, 326–335.
- 21 F. Hayashi, Y. Toda, Y. Kanie, M. Kitano, Y. Inoue, T. Yokoyama, M. Hara and H. Hosono, *Chem. Sci.*, 2013, **4**, 3124–3130.
- 22 H. Fang, S. Wu, T. Ayvali, J. Zheng, J. Fellowes, P.-L. Ho, K. C. Leung, A. Large, G. Held, R. Kato, K. Suenaga, Y. I. A. Reyes, H. V. Thang, H.-Y. T. Chen and S. C. E. Tsang, *Nat. Commun.*, 2023, **14**, 647.
- 23 C. Egawa, T. Nishida, S. Naito and K. Tamaru, *J. Chem. Soc.*, 1984, **80**, 1595.
- 24 W. Tsai and W. H. Weinberg, *J. Phys. Chem.*, 1987, **91**, 5302–5307.
- 25 X. Lu, J. Zhang, W.-K. Chen and A. Roldan, *Nanoscale Adv.*, 2021, **3**, 1624–1632.
- 26 S. Sun, Q. Jiang, D. Zhao, T. Cao, H. Sha, C. Zhang, H. Song and Z. Da, *Renewable Sustainable Energy Rev.*, 2022, **169**, 112918.
- 27 A. S. Chellappa, C. M. Fischer and W. J. Thomson, *Appl. Catal., A*, 2002, **227**, 231–240.
- 28 W. Pyrz, R. Vijay, J. Binz, J. Lauterbach and D. J. Buttrey, *Top. Catal.*, 2008, **50**, 180–191.
- 29 S. Sayas, N. Morlanés, S. P. Katikaneni, A. Harale, B. Solami and J. Gascon, *Catal. Sci. Technol.*, 2020, **10**, 5027–5035.
- 30 S. R. Kulkarni, N. Realpe, A. Yerrayya, V. K. Velisoju, S. Sayas, N. Morlanes, J. Cerillo, S. P. Katikaneni, S. N. Paglieri, B. Solami, J. Gascon and P. Castaño, *Catal. Sci. Technol.*, 2023, **13**, 2026–2037.
- 31 S. Armenise, E. García-Bordejé, J. L. Valverde, E. Romeo and A. Monzón, *Phys. Chem. Chem. Phys.*, 2013, **15**, 12104–12117.
- 32 R. Antunes, R. Steiner, L. Marot and E. Meyer, *Int. J. Hydrogen Energy*, 2022, **47**, 14130–14140.
- 33 K. Aika and A. Ozaki, *J. Catal.*, 1969, **13**, 232–237.
- 34 K. Aika and A. Ozaki, *J. Catal.*, 1970, **19**, 350–352.
- 35 K. Aika and A. Ozaki, *J. Catal.*, 1969, **14**, 311–321.
- 36 Y. Izumi and K. Aika, *J. Phys. Chem.*, 1995, **99**, 10346–10353.
- 37 Y. Izumi, Y. Iwata and K. Aika, *J. Phys. Chem.*, 1996, **100**, 9421–9428.
- 38 P. Stoltze, *J. Catal.*, 1988, **110**, 1–10.
- 39 C. S. Kellner and A. T. Bell, *J. Catal.*, 1981, **67**, 175–185.

